Journal of *Marine Science and Engineering*

MDPI

Article

Experimental Research on Effect of Working-Fluid Flow Rate on OTEC Using Ammonia/Water Mixture

Yasuyuki Ikegami [1], Junichi Inadomi [2], Hirokazu Goto [2] and Takafumi Morisaki [1,*]

[1] Institute of Ocean Energy, Saga University, 1-Honjo machi, Saga-shi, Saga 840-8502, Japan; ikegami@cc.saga-u.ac.jp
[2] Graduate School of Science and Engineering, Saga University, 1-Honjo machi, Saga-shi, Saga 840-8502, Japan; 07533003@edu.cc.saga-u.ac.jp (J.I.); 08533009@edu.cc.saga-u.ac.jp (H.G.)
* Correspondence: morisaki@ioes.saga-u.ac.jp; Tel.: +81-952-28-8624

Abstract

Ocean thermal energy conversion (OTEC) systems using an ammonia/water mixture (AWM) can achieve better thermodynamic performance than comparable single fluid cycles. However, the effects of the working fluid flow rate on the operating pressures, heat exchanger performance, and net power output have not been fully clarified. This study experimentally investigates the effects of the working fluid flow rate (5–12 t/h) and heat source flow rates (400–500 m^3/h) using a 30 kW class OTEC facility equipped with low-pressure drop embossed plate heat exchangers. Increasing the working fluid flow rate enhanced the overall heat transfer coefficients of the evaporator and condenser, but also increased parasitic pumping power and changed the vapor quality at the gas–liquid separator outlet. These competing effects produced a distinct maximum in net power output. Among the tested conditions, the maximum net power output of 15.6 kW was obtained at warm and cold water flow rates of 400 m^3/h and a working fluid flow rate of 6 t/h. These findings demonstrate that the working fluid flow rate must be selected by considering heat transfer enhancement, vapor separation, pressure loss, and auxiliary pumping power simultaneously.

Keywords: ammonia/water mixture; OTEC; working fluid flow rate; embossed plate heat exchanger; net power output

1. Introduction

As global energy and environmental challenges become increasingly severe, ocean thermal energy conversion (OTEC) has attracted considerable attention as a stable source of renewable energy [1]. In addition to continuous power generation, various cogeneration applications, including seawater desalination and deep ocean water utilization, have been actively investigated [2–4]. The fundamental concept of OTEC, first proposed by J. D'Arsonval in 1881, is based on the natural temperature differential of 20–25 °C between warm surface seawater and cold deep seawater. The relative stability of seawater temperatures throughout the year enables OTEC systems to provide a more stable power output than intermittent renewable energy technologies such as solar and wind power [5,6].

However, the available temperature difference is substantially smaller than that in conventional fossil fuel or nuclear power plants; therefore, the theoretical thermal efficiency of the OTEC cycle is inherently low [7]. Moreover, considerable parasitic power is required to operate the seawater and working fluid pumps, and their combined power consumption accounts for a significant fraction of the gross power output [8].

Check for updates

Academic Editor: Luis A. Vega

Received: 4 July 2026
Revised: 2 October 2026
Accepted: 6 October 2026
Published: 10 October 2026

Copyright: © 2026 by the authors. Licensee MDPI, Basel, Switzerland. This article is an open access article distributed under the terms and conditions of the Creative Commons Attribution (CC BY) license.

Historically, closed cycle OTEC systems based on the Rankine cycle and using low boiling point, single component working fluids, such as pure ammonia, have been widely investigated. To improve system performance, the Kalina cycle, which utilizes an ammonia/water mixture as a non-azeotropic working fluid, was introduced [9,10]. In the broader context of low-grade thermal energy recovery, fundamental theoretical and economic evaluations by El-Sayed and Tribus [11], Valdimarsson and Eliasson [12], and Mirolli [13] demonstrated the thermodynamic advantages of this cycle. These investigations were subsequently extended to geothermal and waste heat applications through the energy and exergy analyses of Nasruddin et al. [14], geothermal integration assessments by Guzović et al. [15], thermoeconomic assessments by Mokarram and Mosaffa [16], and mixture modeling by Xu and Goswami [17]. With specific reference to OTEC applications, Uehara et al. [18,19] demonstrated that the use of the Kalina cycle or advanced absorption and extraction cycles reduces the temperature differences within the heat exchangers, thereby significantly improving cycle thermal efficiency compared with that of conventional Rankine cycles.

The Kalina cycle and other mixture cycles have also been implemented in industrial waste heat recovery and geothermal systems [20–22]. Examples include a 3000 kW system using converter furnace cooling water at approximately 98 °C at the Kashima Steel Works of Sumitomo Metal Industries [23], a 4000 kW system using radiant heat from distillation top gas at approximately 110 °C at the Sodegaura Refinery of Fuji Oil, and a 2 MW geothermal power system that operates in Husavik, Iceland [12,24].

Despite these thermodynamic advantages, non-azeotropic mixtures generally exhibit lower heat transfer coefficients than single component fluids during phase change, as reported in previous studies on heat recovery and working fluid mixtures [25,26]. Therefore, realizing the full potential of ammonia/water mixtures requires the optimization of heat exchanger geometries while minimizing hydraulic losses. To address these thermal hydraulic challenges, extensive optimization studies have been conducted in the fields of geothermal energy and industrial low-grade heat recovery. These studies include analyses of flow boiling and pressure drop in plate heat exchangers [27], evaluations of low-grade thermal cycles [28], designs of plate heat exchangers for ammonia [29], and assessments of compact evaporator surfaces by Li et al. [30]. System level efficiency and hydraulic performance have also been investigated through thermodynamic heat recovery analyses [31], parametric optimization of plate heat exchangers [32], and assessments of parasitic hydraulic losses in low-temperature evaporators [33].

Building on the principles established in geothermal and industrial applications, heat exchanger optimization is particularly important for OTEC systems. In OTEC plants, pressure losses in heat exchangers are generally greater than those in the piping network [34,35]. Given the extremely small temperature difference available from ocean thermal resources, the development of high performance heat transfer surfaces that provide a low pressure drop is essential for maximizing net power output. This requirement has been addressed in fundamental studies of OTEC piping and system technologies [36] and in investigations of heat transfer area allocation specifically optimized for OTEC plants [37].

In conventional power plants, cycle thermal efficiency is commonly used as the primary performance indicator. In low-grade heat applications such as OTEC and geothermal power generation, however, the thermal energy and flow rate of the heat source are limited. Therefore, the net power output obtained from a given heat source is a more important performance indicator [38–40]. Thermodynamic optimization studies have shown that varying the working fluid flow rate under fixed heat source conditions creates a trade-off: increasing the working fluid flow rate increases heat absorption but decreases cycle ther-

mal efficiency. Consequently, the relationship between the working fluid flow rate and mechanical power output exhibits a distinct maximum, as illustrated in Figure 1 [41].

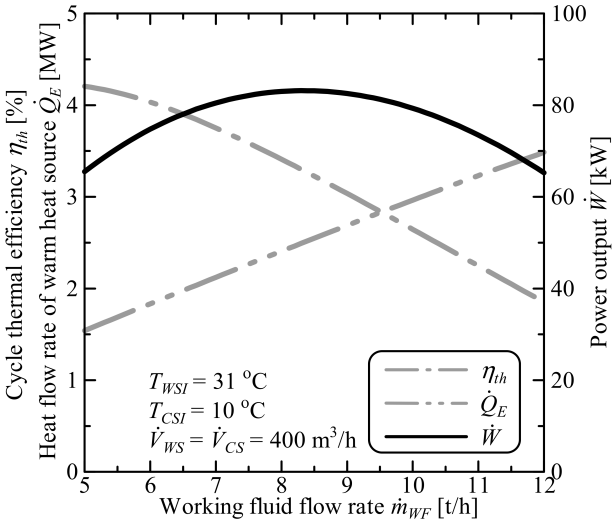


Figure 1. Effects of working fluid flow rate on thermal efficiency of the cycle, evaporator heat flow rate, and power output.

A previous experimental study [34] investigated the effects of the working fluid flow rate and the warm and cold water flow rates on the performance of an ammonia/water OTEC system equipped with a conventional grooved plate evaporator. The results showed that increasing these flow rates could increase the turbine power output but also increased the pumping power requirements. The previous study therefore demonstrated the need for heat exchangers that combine a low-pressure drop with a high overall heat transfer coefficient to improve the net power output and practical feasibility of OTEC systems.

Based on this finding, the present study introduces plate heat exchangers with pyramid shaped embossed surfaces designed to enhance heat transfer while limiting pressure loss. Experiments were conducted using a 30 kW class ammonia/water OTEC facility to investigate the effects of the working fluid and heat source flow rates on the overall heat transfer coefficients, pressure losses, vapor separation behavior, turbine inlet conditions, turbine power output, pumping power output, and net power output. The principal contribution of this study is the experimental identification of the parameters governing turbine and net power performance when the embossed plate heat exchanger configuration is employed. The present and previous experimental systems differ in heat transfer area, separator configuration, internal flow channel geometry, and plate characteristics. Therefore, the results should be interpreted as a system level comparison rather than being attributed solely to differences in embossing geometry.

2. Experimental Apparatus and Methods

2.1. Ocean Thermal Energy Conversion System Using an Ammonia/Water Mixture

Figure 2a shows a schematic flow diagram of the 30 kW class OTEC experimental system operating with an ammonia/water mixture, whereas Figure 2b shows a photograph of the experimental facility. The numerical labels in Figure 2a indicate the thermodynamic state points of the regenerative cycle.

The experimental system consists of an evaporator, a condenser, a gas–liquid separator, a two stage turbine train consisting of two single stage radial flow reaction turbines coupled to a generator, a regenerator, a heater, an after condenser, a pressure reducing

valve, two working fluid pumps, heat source pumps, working fluid storage tanks, and connecting piping.

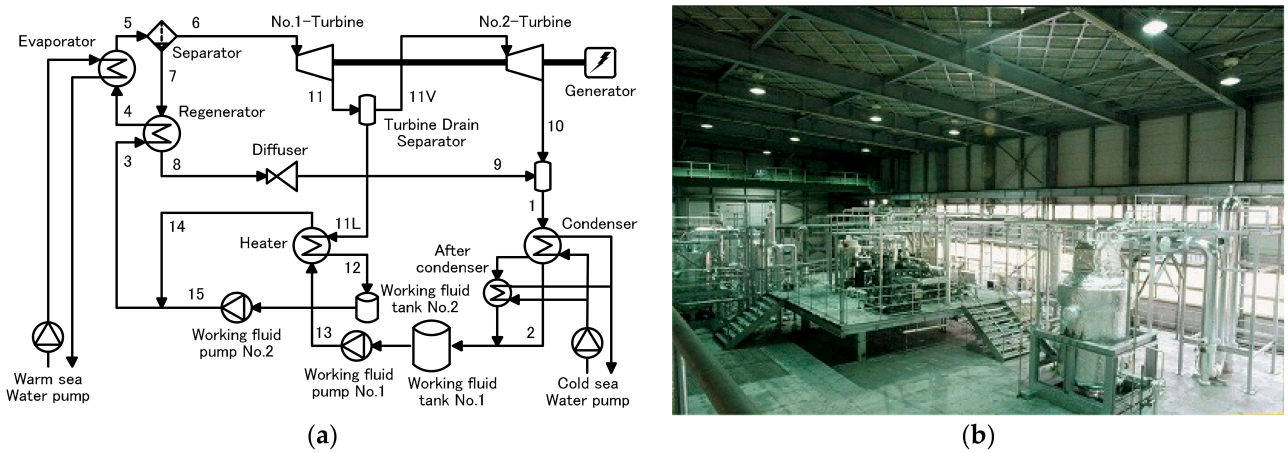


Figure 2. (**a**) Schematic flow diagram of the experimental apparatus; (**b**) photograph of the 30 kW class OTEC experimental plant.

The liquid working fluid is pressurized by working fluid pump No. 1 and supplied to the evaporator through the heater and regenerator (States 13–4). In the evaporator, the working fluid absorbs heat from the warm water and is discharged as a two-phase mixture (States 4–5). The mixture then enters the main gas–liquid separator, where it is separated into saturated vapor and saturated liquid streams (States 5–7).

The vapor separated in the main gas–liquid separator first expands through turbine No. 1 (States 6–11). The wet turbine exhaust at State 11 enters the turbine drain separator, where it is separated into vapor and liquid streams. The separated vapor at State 11V subsequently expands through turbine No. 2 before exiting at State 10. The separated liquid at State 11L passes through the heater and reaches State 12. Meanwhile, the liquid separated in the main gas–liquid separator passes through the regenerator (States 7–8), is depressurized in the pressure reducing valve and diffuser (States 8–9), and then mixes with the exhaust from turbine No. 2 (States 9 and 10–1). The recombined stream enters the condenser (States 1–2).

The main condensate stream is pressurized by working fluid pump No. 1 and then passes through the heater (States 2–13–14). The liquid stream separated in the turbine drain separator passes through the heater (States 11L–12), is collected in working fluid tank No. 2, and is subsequently pressurized by working fluid pump No. 2 (States 12–15). The two liquid streams merge upstream of the regenerator (States 14 and 15–3) and are returned to the evaporator through the regenerator (States 3–4), thereby completing the cycle.

2.2. Heat Exchangers and Component Specifications

The specifications of the main heat exchangers and cycle components are summarized in Tables 1 and 2, respectively. The evaporator and condenser are plate type heat exchangers equipped with titanium plates. The plate surfaces feature pyramid shaped embossing patterns with a nominal embossing height of 5.6 mm, arranged in a staggered pattern. This geometry was selected to enhance fluid mixing while limiting hydraulic resistance. Detailed information regarding the embossing pitch and angle is proprietary and therefore cannot be disclosed. The manufacturer, commercial model, and all non-proprietary dimensions relevant to the thermal hydraulic evaluation are provided in Table 1.

Table 1. Specifications of the main heat exchangers (evaporator and condenser).

Item		Evaporator	Condenser	Evaporator	Condenser
Manufacture		Xenesys Inc., Enzan, Yamanashi, Japan.	Xenesys Inc., Enzan, Yamanashi, Japan.	Xenesys Inc., Enzan, Yamanashi, Japan.	Xenesys Inc., Enzan, Yamanashi, Japan.
Model		A80-40	C3-39	XP28-6A6-050	XP28-6A4-050
Plate Pattern		Herringbone pattern	Herringbone pattern	Pyramid shaped embossed pattern	Pyramid shaped embossed pattern
Plate Material		Titanium	Titanium	Titanium	Titanium
Plate Height	mm	2480	690	1813	1213
Plate Width	mm	690	930	709	709
Plate Thickness	mm	0.6	0.6	0.6	0.6
Number of Plates		320	702	100/module	100/module
Heat Transfer Area	m^2	561.2	464.4	136/module	91.1/module
Equivalent Hydraulic Diameter	mm	0.6	0.6	5.6	5.6

Table 2. Specifications of the principal cycle components.

Component	Specifications/Details
Regenerator	Shell and Plate type (SUS304 shell, Titanium plates, Xenesys Inc., Enzan, Yama-nashi, Japan); 78 plates; Dimensions: 690 mm × 310 mm × 0.6 mm^t; Area: 9.2 m^2; Equivalent diameter: 6.0 mm.
Heater	Shell and Plate type (SUS304 shell, Titanium plates, Xenesys Inc., Enzan, Yama-nashi, Japan); 78 plates; Dimensions: 690 mm × 310 mm × 0.6 mm^t; Area: 9.2 m^2; Equivalent diameter: 6.0 mm.
After Condenser	Shell and Tube type (SUS304 shell, Titanium tubes); tube thickness: 2 mm; number of tubes: 28; tube length: 3.0 m; heat transfer area: 4.0 m^2;; tube inner diameter: 14 mm; internal tube volume: 0.02 m^3.
Turbine	Two stage turbine train consisting of two single stage radial flow reaction turbines (Turbines No. 1 and No. 2; KOBE STEEL, LTD., Kobe, Hyogo, Japan, Model GRT230). The total turbine power output was calculated from the working fluid mass flow rates and specific enthalpy differences using Equation (8).
Generator	Permanent magnet synchronous generator coupled to the turbine train. The electrical power generation output was obtained from the generator. Rated output: 30 kW at 11,800 rpm; speed reduced to 1800 rpm through a reduction gear.
Gas–Liquid Separator	Vertical cylindrical shell (0.7 m diameter, 0.436 m^3 volume) with internal demister.
Working Fluid Pump No. 1	Canned motor pump (TEIKOKU ELECTRIC MFG. CO., LTD., Tatsuno, Hyogo, Japan, Model R42-416C4L/NV-1106). Rated head: 80 m; Flow rate: 400 L/min; Motor power: 11 kW; Inverter flow control.
Working Fluid Pump No. 2	Metering pump (TEIKOKU ELECTRIC MFG. CO., LTD., Tatsuno, Hyogo, Japan, Model ELMs-1). Outlet pressure: 0.85 MPa; Flow rate: 400 L/min; Motor power: 2.2 kW; Inverter controlled.

2.3. Operating State Point Parameters Under Baseline Conditions

Table 3 summarizes the measured working fluid temperatures, pressures, mass flow rates, and phase states at the available state points shown in Figure 2a. The baseline operating condition consisted of a warm water inlet temperature of 31 °C and a warm water flow rate of 400 m^3/h, a cold water inlet temperature of 10 °C and a cold water flow rate of 400 m^3/h, an ammonia mass fraction of 0.98 NH_3 kg/kg mixture, and a total working fluid flow rate of 6 t/h.

Table 3. Working fluid properties at the available state points under the baseline operating condition shown in Figure 2a.

State Point	Description	Temp. [°C]	Press. [MPa]	Mass Flow Rate [kg/s]	Phase/Condition
1	Condenser Inlet	17.0	0.708	1.67	Wet vapor
2	Condenser Outlet	14.8	0.708	1.67	Saturated liquid
3	Regenerator Cold Inlet	18.5	1.005	1.67	Subcooled liquid
4	Evaporator Inlet	27.2	1.001	1.67	Subcooled liquid
5	Evaporator Outlet	27.5	0.985	1.67	Wet vapor
6	Turbine No. 1 Inlet	27.5	0.968	1.25	Saturated vapor
7	Separator Liquid Outlet	27.5	0.985	0.42	Saturated liquid
8	Regenerator Hot Outlet	20.1	0.980	0.42	Subcooled liquid
9	Diffuser Outlet	20.1	0.710	0.42	Subcooled liquid
10	Turbine No. 2 Outlet	17.5	0.710	1.20	Wet vapor
11L	Turbine Drain Separator Liquid Outlet	22.0	0.820	0.05	Saturated liquid
13	Pump No. 1 Outlet	14.9	1.010	1.62	Subcooled liquid

2.4. Measurement Instrumentation

Water heated by a boiler and water cooled by a chiller were used to simulate the warm and cold seawater heat sources, respectively, thereby eliminating the effects of biofouling and fluctuations in natural seawater conditions. Table 4 lists the measured variables, sensor types, manufacturers, model numbers, measurement ranges, and manufacturer specified instrument accuracies.

Table 4. Specifications and accuracies of the measurement instruments.

Measured Variable	Sensor/ Instrument	Manufacture	Model/Type	Measurement Range	Accuracy
Heat Source Temperature	RTD (Pt100)	Hayashidenko Co., Ltd., Bunkyo, Tokyo, Japan	R1-4.8-200L-CF1/2-A	0–50 °C	±0.1 °C
Heat Source Pressure	Pressure Detector	Toshiba Corporation, Minato, Tokyo, Japan	AP3051CD	0–1.5 MPa	±1.1 kPa
Heat Source Volumetric Flow	Electromagnetic Flowmeter	Tokyo Keiso Co., Ltd., Minato, Tokyo, Japan	MGM4510K/ MGM1010K	0–750 m^3/h	±0.5% (±4.13 m^3/h)
Working Fluid Temperature	Sheathed RTD (Pt100)	Hayashidenko Co., Ltd., Bunkyo, Tokyo, Japan	R3N-4.8-150L-RF1-A	0–50 °C	±0.1 °C
Working Fluid Pressure	Pressure Detector	Toshiba Corporation, Minato, Tokyo, Japan	AP3051CG	0–1.5 MPa	±1.1 kPa (±0.075%)
Working Fluid Differential Press.	Differential Pressure Detector	Toshiba Corporation, Minato, Tokyo, Japan	AP3051CG	–248 to +248 kPa	±0.37 kPa
Working Fluid Liquid Flow	Coriolis Mass Flowmeter	Endress+Hauser Sakura Co., Ltd., Fuchu, Tokyo, Japan	Promass 83F50/83F15	0–5.56 kg/s	±0.0056 kg/s (±0.1%)
Working Fluid Liquid Density	Coriolis Mass Flowmeter	Endress+Hauser Sakura Co., Ltd., Fuchu, Tokyo, Japan	Promass 83F50/83F15	500–900 kg/m^3	±1.0 kg/m^3

Temperatures were measured using Pt100 resistance temperature detectors. The heat source flow rates were measured using electromagnetic flowmeters, whereas the

liquid and vapor phase working fluid flow rates were measured using the instruments listed in Table 4. The working fluid pressures and differential pressures were measured using pressure transmitters. The generator power output, $\dot{W}_G$, was measured using the permanent magnet synchronous generator described in Table 2. This measured generator output was distinguished from the turbine power output, $\dot{W}_T$, which was calculated from the working fluid mass flow rates and the corresponding specific enthalpy differences using Equation (8). The calculated turbine power output was used for the subsequent performance evaluations, graphical analyses, and uncertainty analysis.

3. Performance Evaluation Methods

3.1. Performance Evaluation Equations and Data Processing

The measurement signals were recorded at a sampling frequency of 1 Hz. The performance parameters were calculated from 15 min averages of the measured data after the system had reached steady state operation. The thermodynamic properties of the ammonia/water mixture were calculated using M-PROPATH with the property correlations developed by Ibrahim and Klein [42]. The reference state for the specific enthalpy and entropy was defined as the saturated liquid state at 273.15 K, with the reference values set to 200 kJ/kg and 1 kJ/(kg·K), respectively. The mixture composition was expressed in terms of the ammonia mass fraction throughout this study.

The overall heat transfer coefficient, U, was calculated from the heat flow rate, $\dot{Q}$, heat transfer area, A, and logarithmic mean temperature difference (LMTD), ΔT_m, using Equation (1):

$$U = \dot{Q}/(A\ \Delta T_m). \tag{1}$$

The evaporator and condenser heat flow rates, $\dot{Q}_E$ and $\dot{Q}_C$, were calculated using Equations (2) and (3), respectively. In these equations, $\dot{m}_{WS}$ and $\dot{m}_{CS}$ denote the mass flow rates of the warm and cold water; c_{PWS} and c_{PCS} denote their specific heat capacities at constant pressure; T_{WSI} and T_{CSI} denote their inlet temperatures; and T_{WSO} and T_{CSO} denote their outlet temperatures.

$$\dot{Q}_E = \dot{m}_{WS}\ c_{PWS}\ (T_{WSI} - T_{WSO}). \tag{2}$$

$$\dot{Q}_C = \dot{m}_{CS}\ c_{PCS}\ (T_{CSO} - T_{CSI}). \tag{3}$$

The LMTDs for the evaporator and condenser, $(\Delta T_m)_E$ and $(\Delta T_m)_C$, were calculated using Equations (4) and (5), respectively, in accordance with the data reduction method applied to the previous experimental data. In the present analysis, the variation in the temperature difference along each heat exchanger was represented by an effective LMTD derived from the terminal temperatures. For the non-azeotropic ammonia/water mixture, the bubble point temperature at the evaporator inlet, T_{4B}, was used in Equation (4) to account for the onset of boiling and the associated temperature glide.

A single LMTD may not adequately represent the local temperature profile when the temperature difference between the hot and cold streams is very large or when the temperature glide is strongly nonlinear. However, under the relatively small heat source temperature differences typical of OTEC operation, the LMTD method was considered suitable for representing the effective temperature difference and comparing the system level performance of the heat exchangers. A segmented heat exchanger model would be required to analyze the detailed local temperature distribution:

$$(\Delta T_m)_E = [(T_{WSI} - T_5) - (T_{WSO} - T_{4B})]/ln[(T_{WSI} - T_5)/(T_{WSO} - T_{4B})]. \tag{4}$$

$$(\Delta T_m)_C = [(T_1 - T_{CSO}) - (T_2 - T_{CSI})]/ln[(T_1 - T_{CSO})/(T_2 - T_{CSI})]. \tag{5}$$

where T_5 is the working fluid temperature at the evaporator outlet, and T_1 and T_2 are the working fluid temperatures at the condenser inlet and outlet, respectively.

The total mass flow rate of the ammonia/water working fluid at the evaporator inlet, $\dot{m}_{WF}$, was measured directly using a Coriolis mass flowmeter. In the gas–liquid separator, the ammonia mass fractions of the vapor and liquid phases, x_6 and x_7, respectively, were calculated from the measured separator temperature and pressure using M-PROPATH, assuming vapor–liquid equilibrium.

Using the overall ammonia mass fraction at the separator inlet, x_5, the vapor separation ratio, ξ_5, was obtained from the ammonia mass balance as follows:

$$\xi_5 = (x_5 - x_7)/(x_6 - x_7). \tag{6}$$

The vapor mass flow rate at the inlet of the first stage turbine was then calculated as follows:

$$\dot{m}_6 = \xi_5 \, \dot{m}_{WF}. \tag{7}$$

The mass flow rate at the inlet of the second stage turbine, $\dot{m}_{11V}$, was obtained by subtracting the liquid mass flow rate separated by the turbine drain separator, $\dot{m}_{11L}$, from the mass flow rate at the inlet of the first stage turbine, $\dot{m}_6$. The turbine power output, $\dot{W}_T$, was calculated as the sum of the contributions from the high- and low-pressure turbines. The high-pressure turbine power was calculated from the mass flow rate, $\dot{m}_6$, and specific enthalpy difference, $(h_6 - h_{11})$, whereas the low-pressure turbine power was calculated from the mass flow rate, $\dot{m}_{11V}$, and specific enthalpy difference, $(h_{11V} - h_{10})$, as expressed in Equation (8):

$$\dot{W}_T = \dot{m}_6 \, (h_6 - h_{11}) + \dot{m}_{11V} \, (h_{11V} - h_{10}). \tag{8}$$

The total working fluid pump power, $\dot{W}_{PWF}$, was calculated using Equation (9):

$$\dot{W}_{PWF} = \dot{m}_2 \, (h_{13} - h_2) + \dot{m}_{15} \, (h_3 - h_{15}). \tag{9}$$

The system boundary used to calculate the net power output, $\dot{W}_{net}$, included the turbine, the working fluid pumps, and the warm and cold water pumping power requirements resulting from the pressure losses in the principal heat exchangers. External piping losses and the power consumption of minor auxiliary equipment were excluded. Accordingly, the net power output was calculated using Equation (10):

$$\dot{W}_{net} = \dot{W}_T - \dot{W}_{PWS} - \dot{W}_{PCS} - \dot{W}_{PWF}. \tag{10}$$

The warm and cold water pumping powers, $\dot{W}_{PWS}$ and $\dot{W}_{PCS}$, respectively, were calculated using Equations (11) and (12):

$$\dot{W}_{PWS} = \dot{m}_{WS} \, \Delta P_{WS}/(\rho_{WS} \, \eta_{PWS}). \tag{11}$$

$$\dot{W}_{PCS} = \dot{m}_{CS} \, \Delta P_{CS}/(\rho_{CS} \, \eta_{PCS}). \tag{12}$$

The mechanical efficiencies of the warm and cold water pumps, η_{PWS} and η_{PCS}, were both set to 0.85.

The cycle thermal efficiency, η_{th}, theoretical maximum power, $\dot{W}_m$ [43], net power efficiency, η_{net}, and maximum net power efficiency, $\eta_{m,net}$, were calculated using Equations (13)–(16), respectively. Absolute temperatures expressed in kelvin were used for T_{WSI} and T_{CSI} in Equation (14).

$$\eta_{th} = \left(\dot{W}_T - \dot{W}_{PWF}\right)/\dot{Q}_E. \tag{13}$$

$$\dot{W}_m = \left(\sqrt{T_{WSI}} - \sqrt{T_{CSI}}\right)^2 / \left({C_{WS}}^{-1} + {C_{CS}}^{-1}\right). \quad (14)$$

$$\eta_{net} = \dot{W}_{net} / \dot{W}_T. \quad (15)$$

$$\eta_{m,net} = \dot{W}_{net} / \dot{W}_m. \quad (16)$$

3.2. Uncertainty Analysis

To quantify the reliability of the measurements and the derived thermodynamic parameters presented in Section 3.1, an uncertainty propagation analysis was conducted according to the method of Kline and McClintock [44].

The absolute and propagated relative uncertainties in the principal measured variables and derived thermodynamic performance parameters at the baseline operating condition are summarized in Table 5. The measurement uncertainties associated with temperature (±0.1 °C), pressure (±1.1 kPa), and the flow rates (±0.1% to ±0.5%) resulted in propagated relative uncertainties of ±1.82% for the evaporator heat flow rate, $\dot{Q}_E$; ±2.39% for the turbine power output, $\dot{W}_T$; and ±3.13% for the evaporator overall heat transfer coefficient, U_E. The propagated relative uncertainty in the net power output, $\dot{W}_{net}$, was ±2.82%. These uncertainty estimates were smaller than the principal variations observed in the experimental results, supporting the reliability of the trends identified in this study.

Table 5. Uncertainty analysis results of primary measured variables and derived parameters under baseline operating conditions.

Parameter	Symbol	Nominal Value	Absolute Uncertainty	Relative Uncertainty
Warm Water Inlet Temperature	T_{WSI}	31.00 °C	±0.10 °C	±0.32%
Cold Water Inlet Temperature	T_{CSI}	10.00 °C	±0.10 °C	±1.00%
Warm Water Flow Rate	$\dot{V}_{WS}$	400.0 m^3/h	±2.0 m^3/h	±0.50%
Cold Water Flow Rate	$\dot{V}_{CS}$	400.0 m^3/h	±2.0 m^3/h	±0.50%
Working Fluid Flow Rate	m_{WF}	6.00 t/h	±0.006 t/h	±0.10%
Evaporator Inlet Pressure	P_{EI}	1.001 MPa	±0.0011 MPa	±0.11%
Evaporator Heat Rate	Q_E	1.48 MW	±0.027 MW	±1.82%
Condenser Heat Rate	Q_C	1.42 MW	±0.028 MW	±1.97%
Log Mean Temp. Diff. (Evap.)	$(\Delta T_m)_E$	2.85 K	±0.068 K	±2.39%
Overall Heat Transfer Coeff. (Evap.)	U_E	1.15 kW/m^2/K	±0.036 kW/m^2/K	±3.13%
Turbine Power Output	$\dot{W}_T$	32.20 kW	±0.77 kW	±2.39%
Net Power Output	$\dot{W}_{net}$	15.60 kW	±0.44 kW	±2.82%
Cycle Thermal Efficiency	η_{th}	1.52%	±0.046%	±3.03%

The uncertainty in the turbine power output, $\dot{W}_T$, was determined by propagating the uncertainties in the working fluid mass flow rates and specific enthalpies used in Equation (8). The measured generator power output, $\dot{W}_G$, was not used in the calculation of either the turbine power output or its associated uncertainty.

4. Experimental Conditions

The experimental conditions are summarized in Table 6. Two sets of experiments were conducted. First, the results obtained in Case-I, using a frame-and-plate evaporator equipped with embossed plates, were compared with those obtained in Case-II by Yasunaga et al. [34], who used a shell-and-plate evaporator equipped with herringbone plates. Under the conditions used for this comparison, the warm water inlet temperature and flow rate were 29 °C and 500 m^3/h, respectively, whereas the cold water inlet temperature and flow rate were 8 °C and 400 m^3/h, respectively. The ammonia mass fraction was 0.95 NH_3 kg/kg

mixture. Case-I used four evaporator modules with a total heat transfer area of 544.8 m^2 and three condenser modules with a total heat transfer area of 273.3 m^2. Case-II used a shell-and-plate evaporator with a total heat transfer area of 561.2 m^2 [34].

Table 6. Experiment conditions.

Item		Unit	Value
Warm water evaporator inlet	temperature	°C	29, 31
	flowrate	m^3/h	400, 500
Cold water condenser inlet	temperature	°C	8, 10
	flow rate	m^3/h	400, 500
Number of evaporator modules			3, 4
Number of condenser modules			3
Evaporator inlet ammonia mass fraction $NH_3/(H_2O + NH_3)$		kg/kg	0.95, 0.98
Mass flow rate of working fluid		t/h	5, 6, 7, 8, 9, 10, 12

Second, the effects of the working fluid and heat source flow rates were investigated using three evaporator modules with a total heat transfer area of 408.6 m^2. For this series of experiments, the baseline operating condition consisted of a warm water inlet temperature of 31 °C and a warm water flow rate of 400 m^3/h, a cold water inlet temperature of 10 °C and a cold water flow rate of 400 m^3/h, and an ammonia mass fraction of 0.98 NH_3 kg/kg mixture. The total working fluid flow rate varied from 5 to 12 t/h using the discrete values listed in Table 6. When the warm water flow rate varied, the cold water flow rate was maintained at the baseline value. Conversely, when the cold water flow rate varied, the warm water flow rate was maintained at the baseline value.

5. Results and Discussion

5.1. Comparison of Evaporator Configurations and Effects of Working Fluid Flow Rate

This section presents the experimental results obtained using an ammonia mass fraction of 0.95 NH_3 kg/kg mixture, a warm water inlet temperature of 29 °C, a warm water flow rate of 500 m^3/h, a cold water inlet temperature of 8 °C, and a cold water flow rate of 400 m^3/h. The system level performance of the embossed plate evaporator used in Case-I was compared with that of the shell-and-plate evaporator equipped with herringbone plates used in Case-II, which was previously investigated by Yasunaga et al. [34]. The two cases differ in heat transfer area, gas–liquid separator configuration, internal flow channel geometry, and plate characteristics; therefore, this comparison cannot isolate the effect of the embossing geometry. The results should instead be interpreted as a comparison between the two complete experimental configurations.

Figure 3 shows the turbine power output, $\dot{W}_T$, and evaporator heat flow rate, $\dot{Q}_E$, as functions of the total working fluid flow rate, $\dot{m}_{WF}$. Solid symbols represent Case-I, whereas open symbols represent Case-II [34]. In both cases, $\dot{W}_T$ increases with $\dot{m}_{WF}$ and approaches a plateau at higher flow rates. Case-I exhibits a slightly higher turbine power output than Case-II throughout the tested range. In Case-I, $\dot{Q}_E$ increases with $\dot{m}_{WF}$ up to approximately 8 t/h and remains nearly constant thereafter. By contrast, $\dot{Q}_E$ in Case-II varies only slightly throughout the tested range.

To clarify the factors governing the turbine power output, Figure 4 shows the working fluid flow rate at the turbine inlet, $\dot{m}_{TH}$, and the vapor separation ratio, ξ_5, whereas Figure 5 shows the temperature difference, ΔT_T, and pressure difference, ΔP_T, across the turbine. As $\dot{m}_{WF}$ increases, ξ_5 decreases, indicating a lower vapor fraction at the evaporator outlet. Although the total working fluid flow rate increases, the decrease in ξ_5 limits the increase in $\dot{m}_{TH}$, which approaches a plateau above approximately 8 t/h. In Case-I, ΔT_T and ΔP_T

remain nearly constant throughout the tested range. In Case-II, both parameters initially increase with $\dot{m}_{WF}$ and then stabilize. The combined effects of the turbine inlet flow rate and the pressure and temperature differences across the turbine account for the observed trend in $\dot{W}_T$. The lower $\dot{m}_{TH}$ and vapor separation ratio in Case-II are consistent with its lower turbine power output; however, the individual contributions of the differences between the two system configurations cannot be isolated in the present comparison.

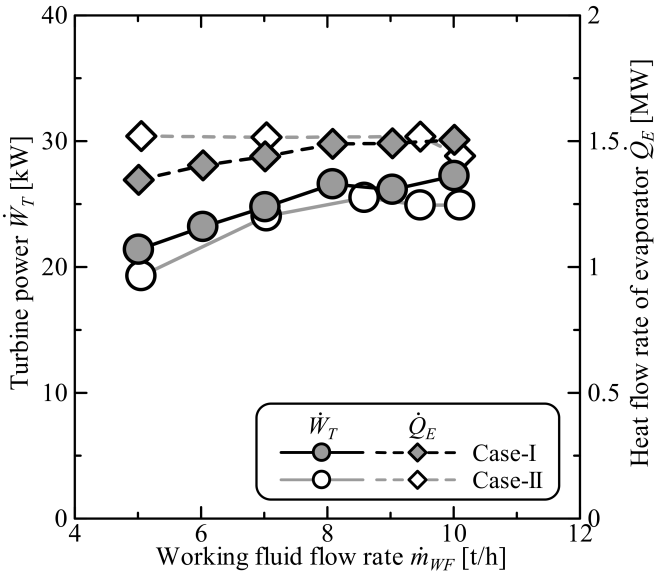


Figure 3. Effects of working fluid flow rate on turbine power and evaporator heat flow rate.

In the ammonia/water OTEC cycle, not all of the working fluid passes through the turbine. The fluid supplied to the evaporator exits as a two-phase mixture and enters the gas–liquid separator. Only the separated vapor is directed to the turbine, whereas the separated liquid is routed to the regenerator. The vapor separation ratio, ξ_5, is defined as the vapor flow rate divided by the total working fluid flow rate at the separator inlet. As shown in Figure 4, ξ_5 decreases as $\dot{m}_{WF}$ increases. This decrease offsets the increase in the total flow rate and causes $\dot{m}_{TH}$ to approach a plateau above approximately 8 t/h.

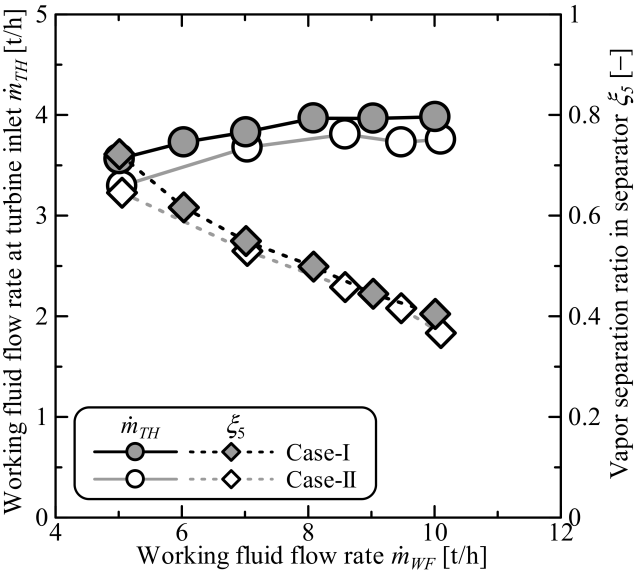


Figure 4. Effects of working fluid flow rate on turbine inlet working fluid flow rate and vapor separation ratio.

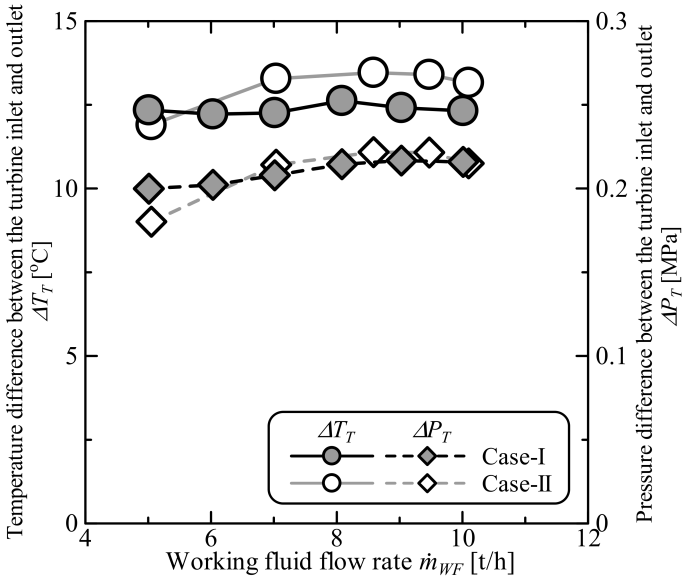


Figure 5. Effects of working fluid flow rate on temperature difference and pressure difference across the turbine inlet and outlet.

Figure 6 shows the working fluid pressures at the evaporator inlet, P_{EI}, evaporator outlet, P_{EO}, and turbine inlet, P_{TH}. The difference between P_{EO} and P_{TH} represents the pressure loss between the evaporator outlet and the turbine inlet, including that occurring in the gas–liquid separator. In Case-I, all three pressures increase with $\dot{m}_{WF}$. Although P_{EI} is higher in Case-I than in Case-II, P_{TH} approaches the Case-II value owing to the pressure losses in the evaporator and separator. The pressure difference between P_{EO} and P_{TH} also increases with $\dot{m}_{WF}$ in Case-I. In Case-II, the shell-and-plate evaporator also functions as a separator; consequently, the separator related pressure loss is smaller than that in Case-I.

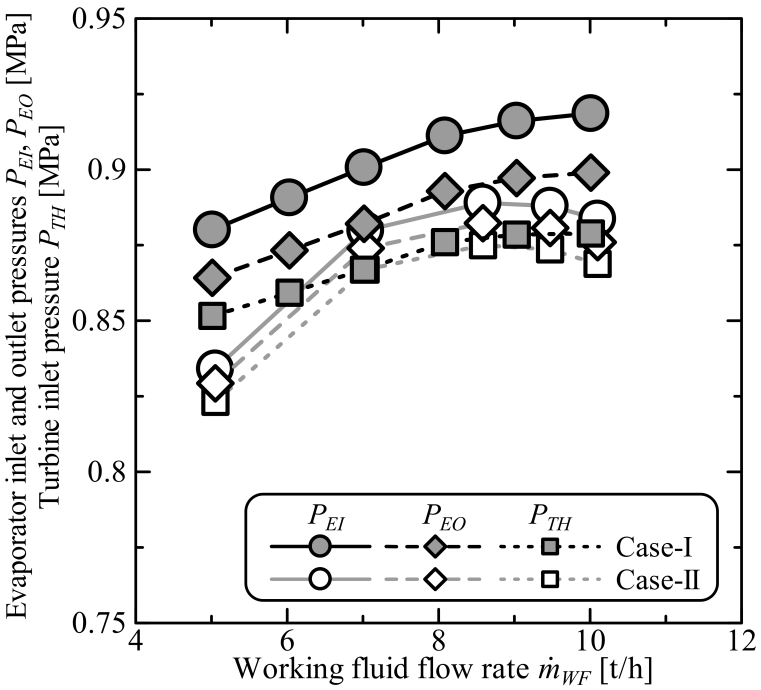


Figure 6. Effects of working fluid flow rate on evaporator inlet pressure, evaporator outlet pressure, and turbine inlet pressure.

Figure 7 shows the working fluid temperatures at the evaporator inlet, T_4, and outlet, T_5. In Case-I, T_5 decreases as the flow rate increases from 5 to 6 t/h and remains nearly constant at higher flow rates, whereas T_5 is nearly independent of $\dot{m}_{WF}$ in Case-II. In both cases, T_4 increases with $\dot{m}_{WF}$ and approaches a plateau at approximately 8 t/h. The evaporator inlet temperature is affected by heat recovery in the regenerator, which depends on the liquid flow rate separated from the two-phase mixture at the evaporator outlet. Thus, T_4 and T_5 are thermodynamically coupled through the separator and regenerator. The observed increase in T_4 is primarily associated with the increase in the total working fluid flow rate and the corresponding change in separator performance. The higher T_5 observed in Case-II may reflect differences in heat transfer area, flow channel geometry, and separator configuration; therefore, this difference should not be attributed solely to the plate surface geometry.

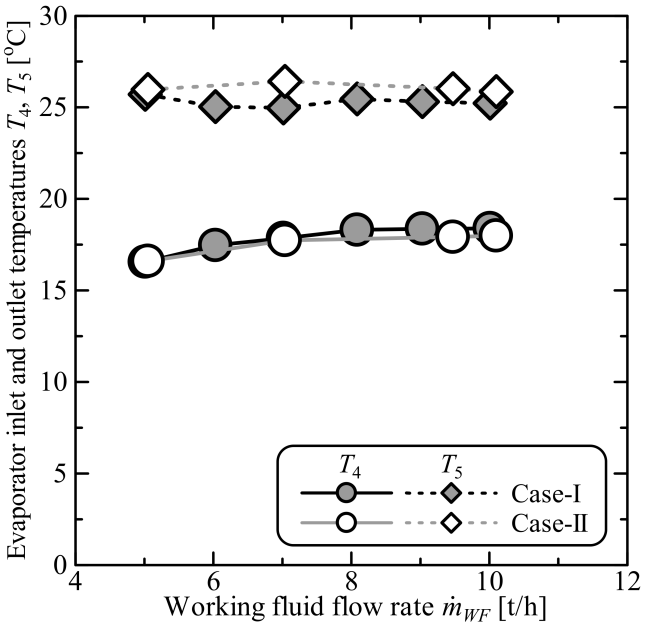


Figure 7. Effects of working fluid flow rate on working fluid temperatures at the evaporator inlet and outlet.

Figure 8 shows the working fluid pressures at the condenser inlet, P_{CI}, and outlet, P_{CO}. Both pressures increase slightly with $\dot{m}_{WF}$ and become nearly constant above approximately 7 t/h. No appreciable pressure difference across the condenser was observed under the tested conditions. The condenser pressure is lower in Case-II than in Case-I, which is consistent with the lower high-pressure side operating pressure in Case-II.

Figure 9 shows the overall heat transfer coefficients of the evaporator and condenser, U_E and U_C, respectively. The Case-II evaporator value at a working fluid flow rate of 8.5 t/h was omitted for the reason described in the discussion in Figure 3. For both heat exchangers, U generally increases with $\dot{m}_{WF}$. The heat transfer resistance on the working fluid side is expected to be greater than that on the water side. Therefore, the increase in U is attributed primarily to the increased mass flux on the working fluid side.

Figures 10–12 summarize the effects of $\dot{m}_{WF}$ on the parasitic pumping power and cycle performance parameters. Figure 10 shows the working fluid pump power, $\dot{W}_{PWF}$, and warm water pump power, $\dot{W}_{PWS}$. The working fluid pump power increases with $\dot{m}_{WF}$ in both cases. In Case-I, $\dot{W}_{PWS}$ remains approximately constant because the warm water flow rate is fixed. In Case-II, however, $\dot{W}_{PWS}$ varies substantially with $\dot{m}_{WF}$. This variation is associated with deformation of the heat exchanger plates, which changes the flow channel area on the heat source side and the corresponding pressure drop. Figure 11

shows that the cycle thermal efficiency, η_{th}, increases with $\dot{m}_{WF}$ and then approaches a plateau. Figure 12 shows that the net power efficiency, η_{net}, in Case-I follows a similar trend and remains nearly constant above approximately 8 t/h. In Case-II, η_{net} fluctuates because of the variation in the warm water pumping power. These results demonstrate that the apparent advantage of increasing the working fluid flow rate is limited by the accompanying increase in parasitic power consumption and the plateau in the vapor flow rate at the turbine inlet.

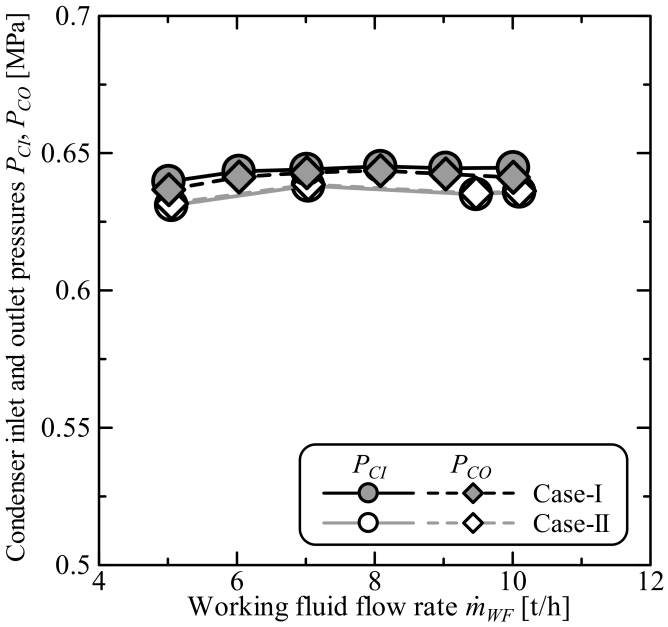


Figure 8. Effects of working fluid flow rate on condenser inlet and outlet pressures.

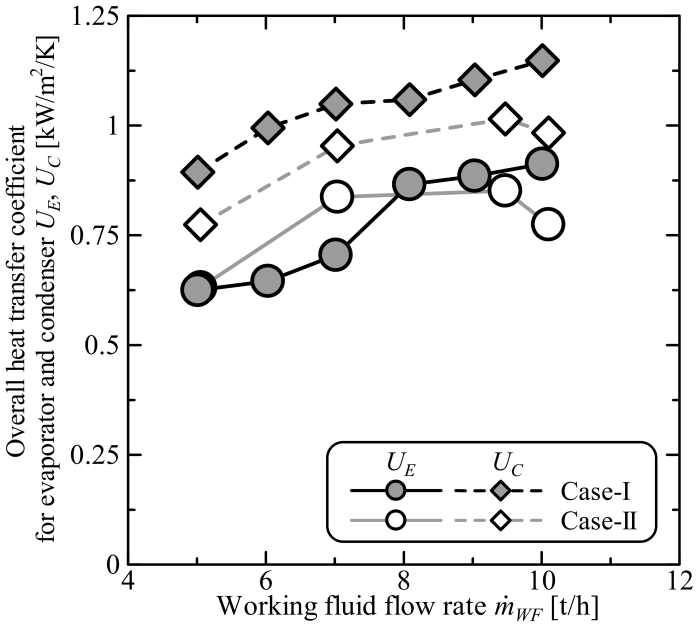


Figure 9. Effects of working fluid flow rate on overall heat transfer coefficients for evaporator and condenser.

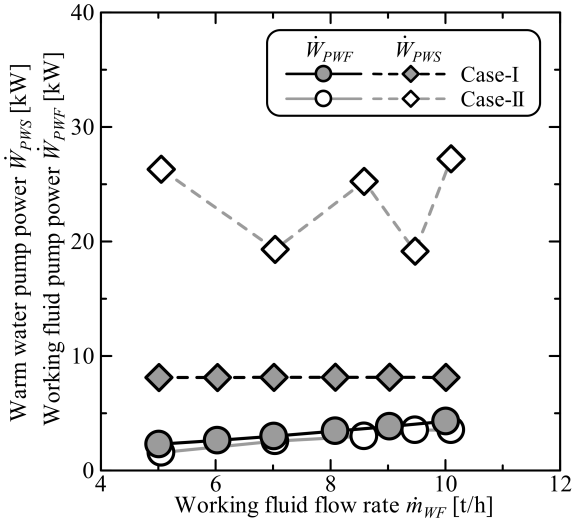


Figure 10. Effects of working fluid flow rate on parasitic power consumption of working fluid and warm water pumps.

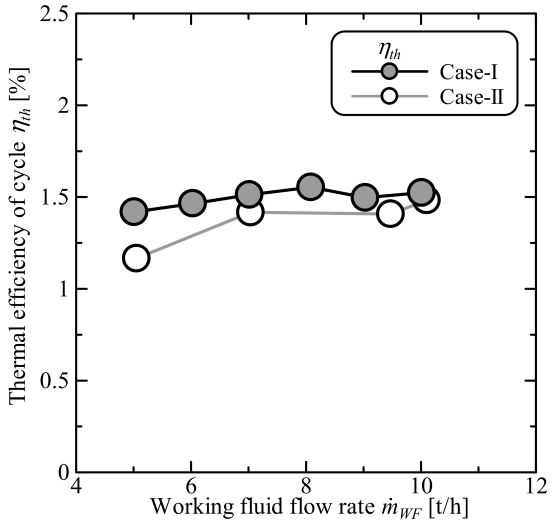


Figure 11. Effects of working fluid flow rate on cycle thermal efficiency.

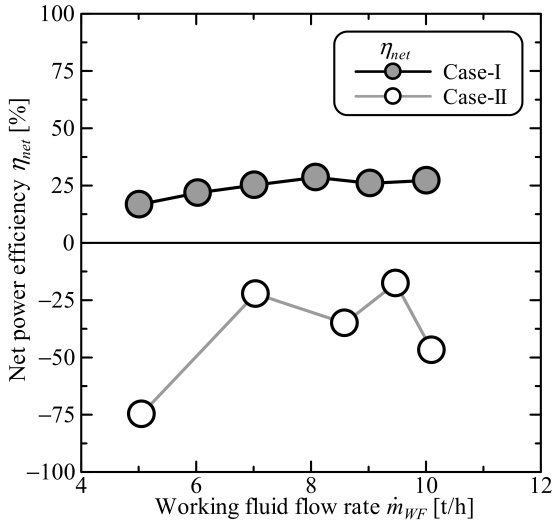


Figure 12. Effects of working fluid flow rate on net power efficiency.

5.2. Effects of Working Fluid and Heat Source Flow Rates

This section examines the combined effects of the working fluid and heat source flow rates. The ammonia mass fraction was 0.98 NH_3 kg/kg mixture, the warm water inlet temperature was 31 °C, and the cold water inlet temperature was 10 °C. The warm and cold water flow rates varied between 400 and 500 m^3/h. The condition in which both water flow rates were set to 400 m^3/h is referred to as the baseline heat source condition.

Figure 13 shows the turbine power output, $\dot{W}_T$, and net power output, $\dot{W}_{net}$, as functions of $\dot{m}_{WF}$ for the three combinations of heat source flow rates. Increasing either the warm or cold water flow rate increases $\dot{W}_T$ relative to the baseline condition. However, $\dot{W}_{net}$ decreases because the increase in heat source pumping power exceeds the increase in turbine power. Increasing either heat source flow rate raises $\dot{W}_T$ by approximately 10%, but the heat source pumping power increases more rapidly. Consequently, the net power output decreases at higher heat source flow rates. Among the discrete working fluid flow rates tested (5, 6, 7, 8, 9, 10, and 12 t/h), the highest net power output was obtained at 6 t/h under the specified heat source conditions.

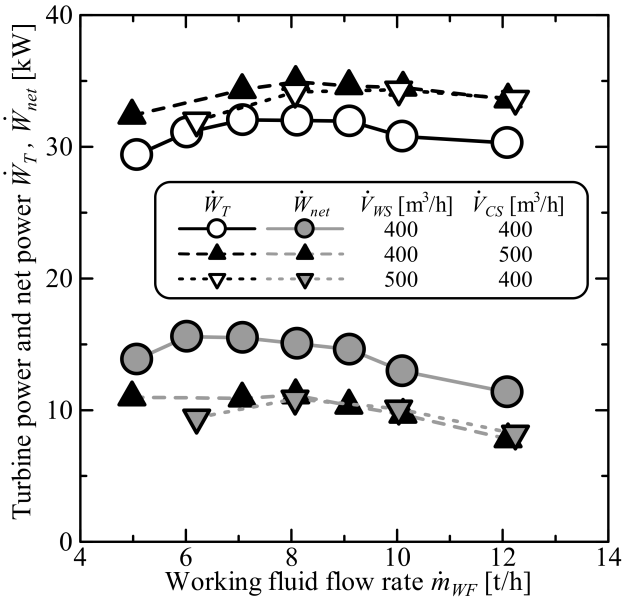


Figure 13. Effects of working fluid and heat source flow rates on turbine power, W_T, and net power output, W_{net}.

Figures 14 and 15 show $\dot{Q}_E$ and the variations in $\dot{m}_{TH}$ and ξ_5, respectively. Both $\dot{Q}_E$ and $\dot{m}_{TH}$ increase with $\dot{m}_{WF}$, whereas ξ_5 decreases. The similar trends observed for $\dot{Q}_E$ and $\dot{m}_{TH}$ indicate that the increase in the mass flux on the working fluid side enhances heat absorption in the evaporator and increases the vapor flow rate supplied to the turbine. Nevertheless, the decrease in ξ_5 limits the increase in $\dot{m}_{TH}$ at higher total working fluid flow rates. Figure 16 shows that ΔT_T and ΔP_T are larger when either the warm or cold water flow rate is increased from its baseline value. These changes contribute to the higher turbine power output observed in Figure 13.

Figures 17 and 18 show the evaporator temperatures and pressures, respectively. As $\dot{m}_{WF}$ increases, the evaporator inlet temperature, evaporation pressure, and turbine inlet pressure increase, whereas the evaporator outlet temperature decreases. The higher pump discharge pressure increases the evaporator pressure, whereas the lower outlet temperature is associated with a decrease in the vapor fraction at the evaporator outlet. The same general trend is observed for all three combinations of heat source flow rates. Above approximately 8 t/h, $\dot{m}_{TH}$ no longer increases appreciably, whereas the pressure

loss between the evaporator outlet and the turbine inlet continues to affect the turbine inlet conditions. This behavior indicates that the pressure loss in the gas–liquid separator becomes increasingly important at higher values of $\dot{m}_{WF}$.

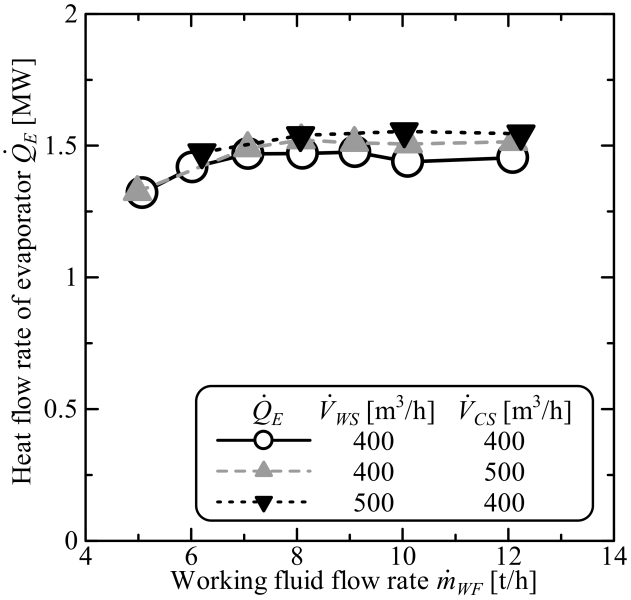


Figure 14. Effects of working fluid flow rate on evaporator heat flow rate, Q_E.

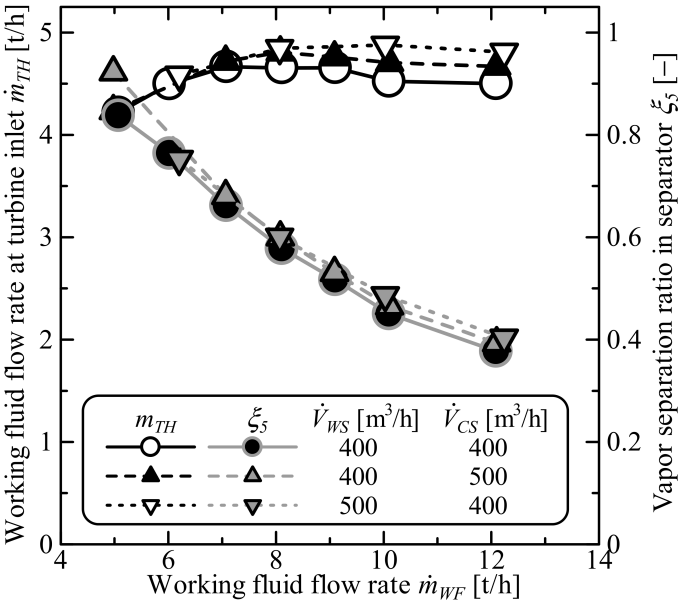


Figure 15. Effects of working fluid flow rate on turbine flow rate, m_{TH}, and vapor separation ratio, ξ_5.

Figure 19 shows the evaporator temperature differences, $\Delta T_{E1} = T_{sat,E} - T_4$ and $\Delta T_{E2} = T_5 - T_{sat,E}$, where $T_{sat,E}$ is the saturated liquid temperature calculated from the working fluid pressure and composition. The value of ΔT_{E2} represents the temperature difference between the two-phase working fluid at the evaporator outlet and the corresponding saturated liquid temperature. The value of ΔT_{E2} decreases as $\dot{m}_{WF}$ increases. The larger value at lower $\dot{m}_{WF}$ contributes to the effective temperature difference during phase change and may partly explain the lower overall heat transfer coefficient observed at low flow rates.

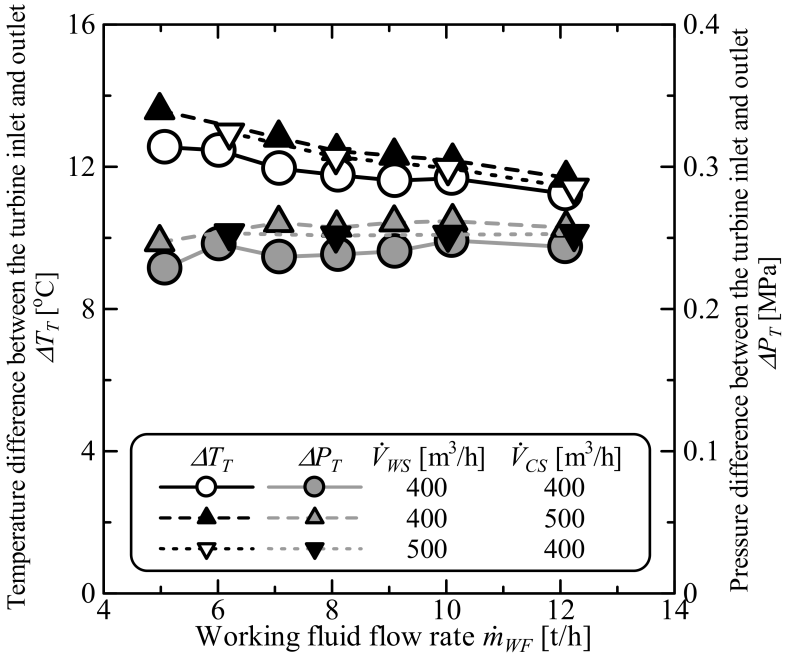


Figure 16. Effects of working fluid flow rate on temperature and pressure differences in turbine, ΔT_T and ΔP_T.

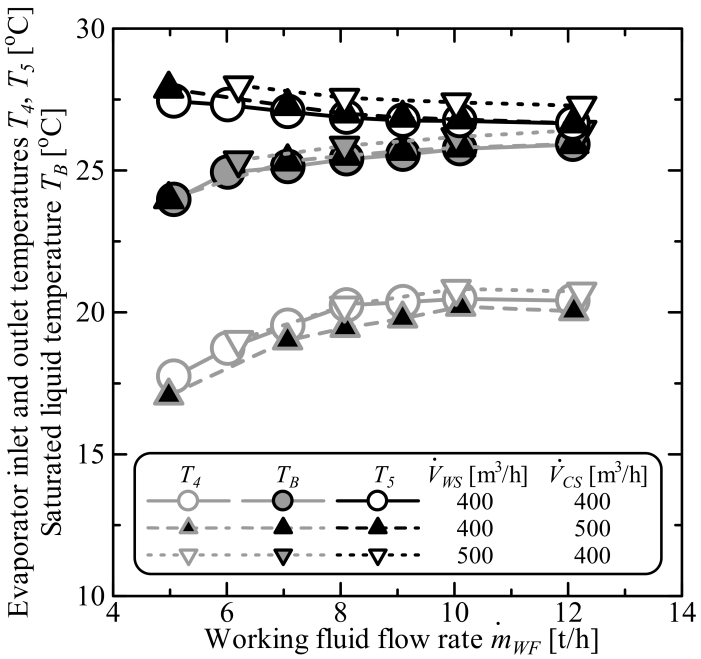


Figure 17. Effects of working fluid flow rate on saturated liquid temperature, T_B, and evaporator inlet and outlet temperatures, T_4 and T_5.

Figures 20 and 21 show the condenser pressures and temperatures, respectively. As $\dot{m}_{WF}$ increases, the condensation pressure and condenser outlet temperature increase, whereas the condenser inlet temperature decreases. The lower inlet temperature is associated with a decrease in the evaporator outlet temperature, whereas the higher condensation pressure reflects the increase in the high-pressure side operating pressure. The thermodynamic state at the condenser outlet was calculated from the measured pressure, temperature, and ammonia mass fraction. These calculations confirmed that the working fluid was completely condensed under all steady state experimental conditions, although the resulting

liquid was only slightly subcooled. The stable circulation of the working fluid and stable operation of the overall system provided additional confirmation of complete condensation at the condenser outlet. The after condenser was used to completely condense any residual vapor during transient operation. The small measured pressure difference between the condenser inlet and outlet is therefore reported as an experimental observation rather than being attributed solely to the working fluid phase state.

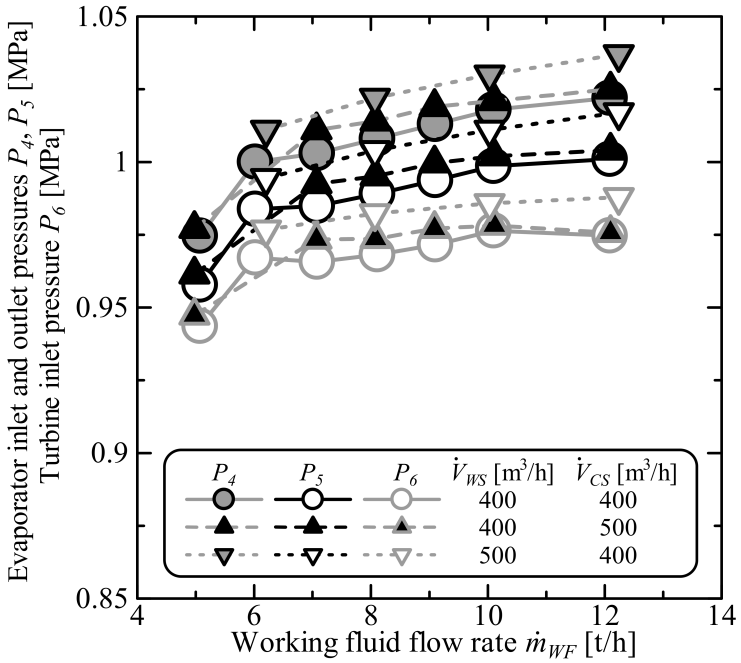


Figure 18. Effects of working fluid flow rate on evaporator inlet and outlet pressures, P_4 and P_5, and turbine inlet pressure, P_6.

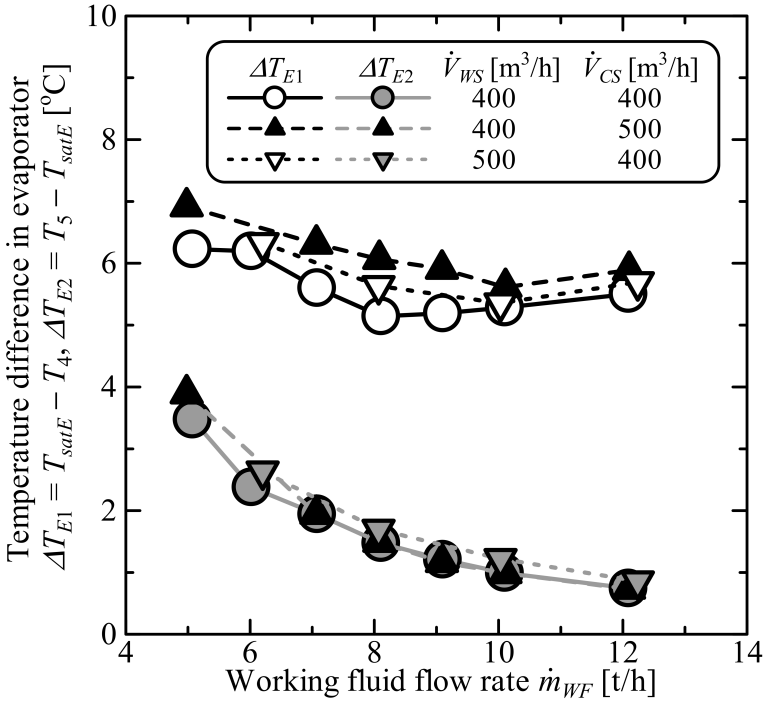


Figure 19. Effects of working fluid flow rate on temperature differences in the evaporator, ΔT_{E1} and ΔT_{E2}.

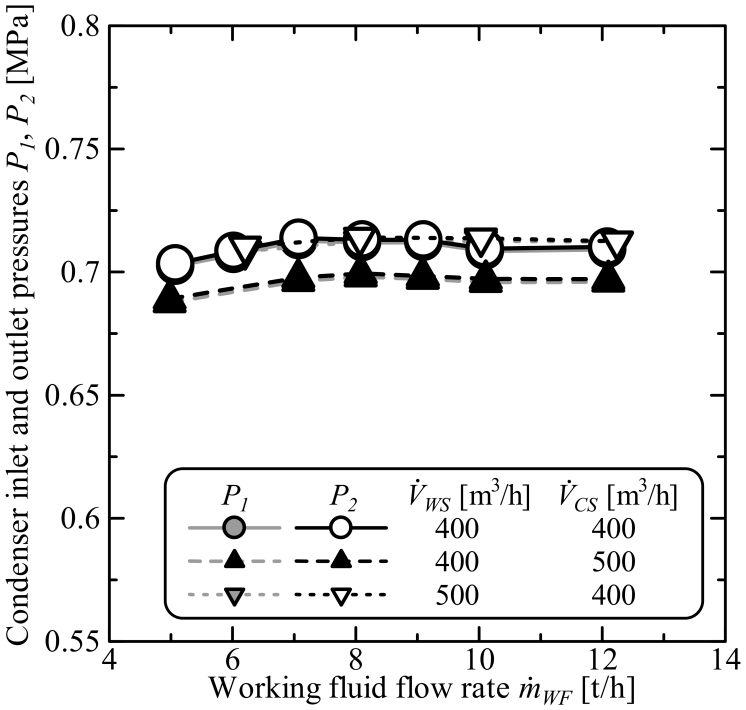


Figure 20. Effects of working fluid flow rate on condenser inlet and outlet pressures, P_1 and P_2.

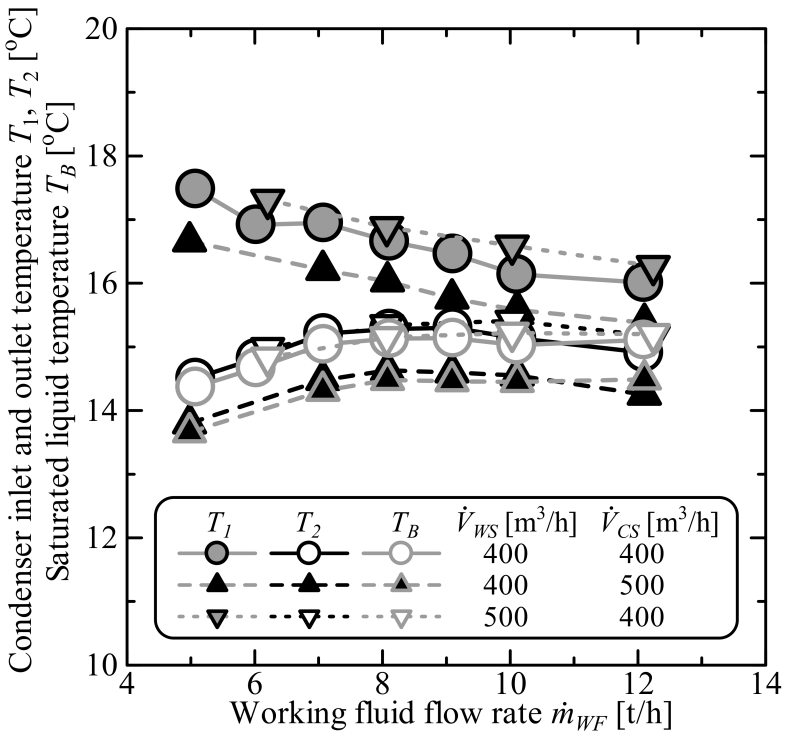


Figure 21. Effects of working fluid flow rate on saturated liquid temperature, T_B, and condenser inlet and outlet temperatures, T_1 and T_2.

Increasing the warm water flow rate raises the evaporation pressure and temperature, whereas increasing the cold water flow rate lowers the condensation pressure and temperature. Both changes increase ΔP_T and ΔT_T across the turbine relative to the baseline condition. The increase in ΔP_T is only smaller when the warm water flow rate is increased compared to when only the cold water flow rate is increased. One possible explanation is

that the increased pressure loss in the gas–liquid separator limits the increase in the turbine inlet pressure under the higher warm water flow condition.

Figure 22 shows the condenser temperature differences, $\Delta T_{C1} = T_1 - T_{sat,C}$ and $\Delta T_{C2} = T_2 - T_{sat,C}$, where $T_{sat,C}$ is the saturated vapor temperature calculated from the working fluid pressure and composition. The value of ΔT_{C1} represents the temperature decrease required for the vapor entering the condenser to reach the saturated vapor state. The value of ΔT_{C1} decreases as $\dot{m}_{WF}$ increases. The larger temperature difference at lower $\dot{m}_{WF}$ may contribute to the lower effective overall heat transfer coefficient under these conditions.

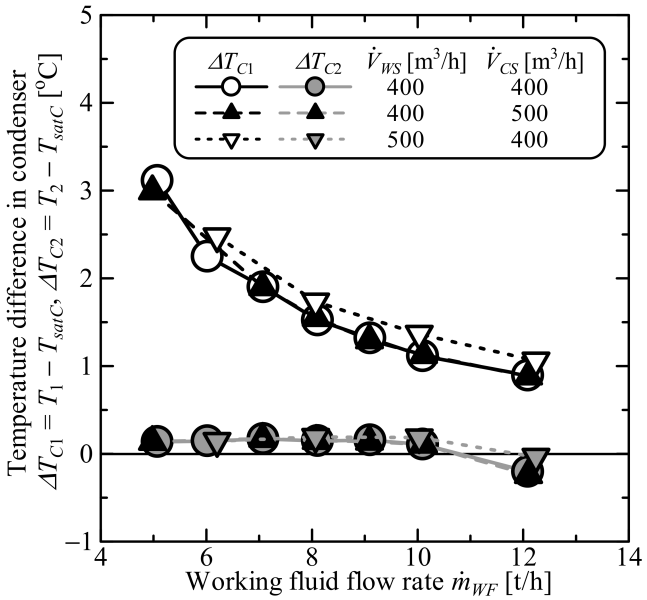


Figure 22. Effects of working fluid flow rate on temperature differences in the condenser, ΔT_{C1} and ΔT_{C2}.

Figures 23–25 show the terminal temperature differences, LMTDs, and overall heat transfer coefficients of the evaporator and condenser. At $\dot{m}_{WF}$ = 5 t/h, the temperature difference between the heat source outlet and the working fluid outlet is small because the working fluid undergoes a relatively large temperature change. In the evaporator, this terminal temperature difference increases with $\dot{m}_{WF}$, whereas the corresponding temperature difference in the condenser decreases above a certain flow rate. The LMTDs of both heat exchangers generally decrease as $\dot{m}_{WF}$ increases. By contrast, U_E and U_C generally increase with $\dot{m}_{WF}$, which is consistent with enhanced convective heat transfer on the working fluid side resulting from the higher mass flux. At the same time, the temperature glide of the ammonia/water mixture decreases as $\dot{m}_{WF}$ increases, thereby reducing some of the thermodynamic advantage associated with non-isothermal phase change.

Figure 26 shows the net power efficiency, η_{net}, and maximum net power efficiency, $\eta_{m,net}$. Both indices are higher at lower heat source flow rates because of the lower heat source pumping power requirements. Under the baseline heat source condition, η_{net} reaches its highest value at $\dot{m}_{WF}$ = 6 t/h and decreases at higher working fluid flow rates. Thus, although the overall heat transfer coefficients improve with $\dot{m}_{WF}$, the highest net power output and net power efficiency among the tested conditions were obtained at 6 t/h. The observed trade off may also be relevant to other low-temperature binary cycle systems, although its applicability to geothermal and industrial waste heat systems requires independent validation.

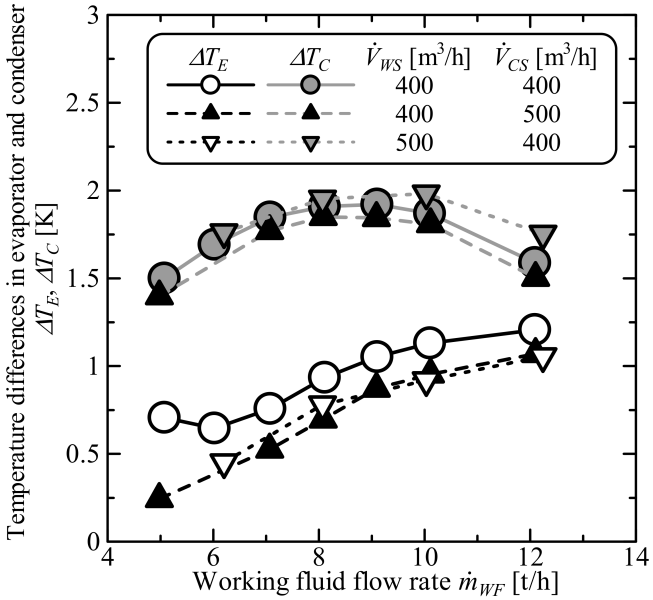


Figure 23. Effects of working fluid flow rate on temperature differences, ΔT_E and ΔT_C.

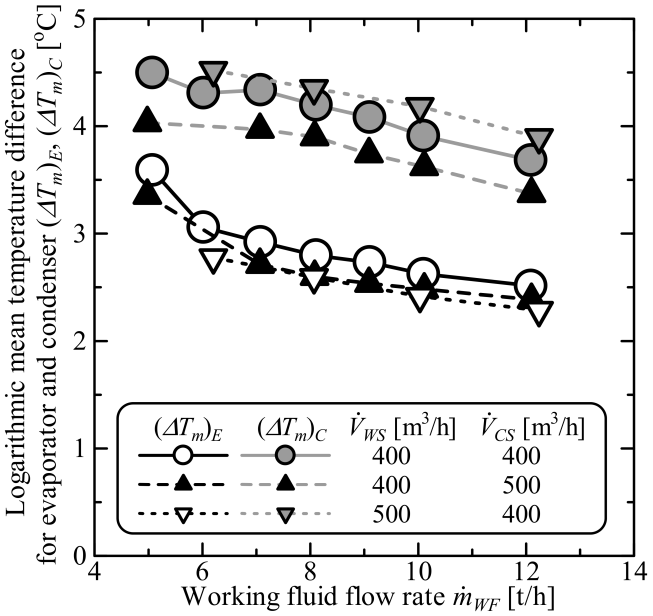


Figure 24. Effects of working fluid flow rate on logarithmic mean temperature differences, $(\Delta T_m)_E$ and $(\Delta T_m)_C$.

The quantitative contribution of the present study can be summarized by the coupled thermal hydraulic performance of the system equipped with pyramid embossed plate heat exchangers. Under the representative baseline condition, at warm and cold water flow rates of 400 m^3/h and a working fluid flow rate of 6 t/h, the evaporator overall heat transfer coefficient, turbine power output, and net power output were 1.15 kW/(m^2·K), 32.2 kW, and 15.6 kW, respectively. The 16.6 kW difference between the turbine and net power outputs represents the combined working fluid and heat source pumping power requirements included within the defined system boundary. Increasing either heat source flow rate from 400 to 500 m^3/h increased the turbine power output by approximately 10%; however, the increase in pumping power exceeded the increase in turbine power, resulting in a lower net power output.

Among the discrete working fluid flow rates tested (5, 6, 7, 8, 9, 10, and 12 t/h), the highest net power output was obtained at 6 t/h. Although the overall heat transfer coefficients generally increased with the working fluid flow rate, the vapor flow rate at the turbine inlet approached a plateau above approximately 8 t/h because the calculated vapor separation ratio decreased. Simultaneously, the working fluid pumping power requirement increased. These results quantitatively demonstrate that maximizing the overall heat transfer coefficient alone does not maximize the net power output. Instead, the working fluid flow rate must be selected by simultaneously considering heat transfer enhancement, pressure losses, vapor separation behavior, turbine inlet conditions, and auxiliary pumping power.

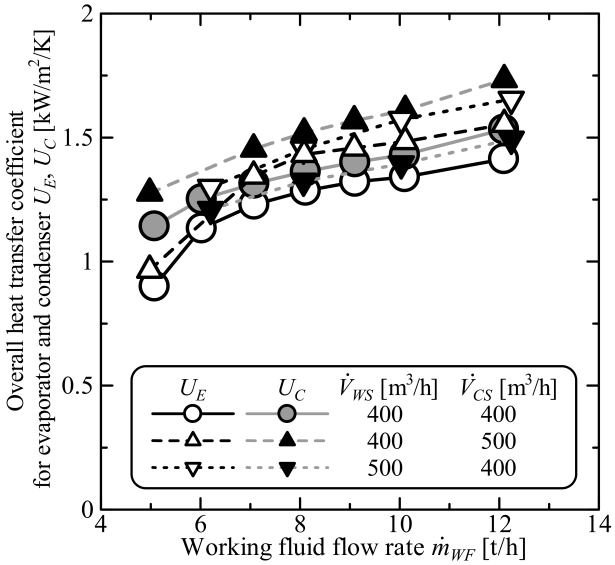


Figure 25. Effects of working fluid flow rate on overall heat transfer coefficients, U_E and U_C.

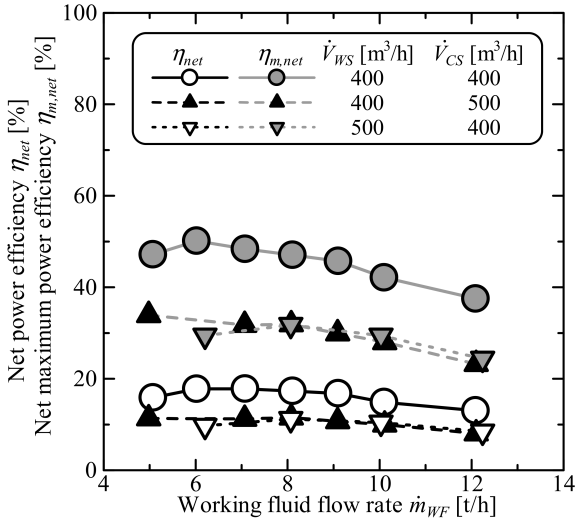


Figure 26. Effects of working fluid flow rate on net power efficiency, η_{net}, and maximum net power efficiency, η_m.

The present results provide practical guidance for the operation and design of ammonia/water OTEC systems. As shown in Figure 13, increasing either the warm or cold water flow rate from 400 to 500 m^3/h increased the turbine power output by approximately 10% but reduced the net power output because the additional heat source pumping power requirement exceeded the increase in turbine power. Therefore, operating the heat source

pumps at their maximum flow rates is not necessarily advantageous. A practical control strategy should optimize the warm water, cold water, and working fluid flow rates in real time to maximize the net power output, rather than maximizing the turbine power output or overall heat transfer coefficient alone. Under the tested conditions, a working fluid flow rate of 6 t/h provided the highest net power output, whereas the vapor flow rate at the turbine inlet approached a plateau above approximately 8 t/h as the vapor separation ratio decreased. These trends indicate that further increases in the working fluid flow rate mainly increase the pumping power requirement without a proportional increase in the flow rate through the turbine. For plant design, heat exchangers should therefore be selected by considering both heat transfer performance and pressure loss, and variable speed pumps should be coordinated based on the measured temperatures, pressures, flow rates, and separator conditions. The specific operating point identified here is applicable only to the present apparatus; however, the demonstrated control criterion—the maximization of net power output after accounting for auxiliary pumping power—is directly applicable to the development of operating strategies for practical OTEC plants.

6. Conclusions

This study experimentally investigated the effects of the working fluid and heat source flow rates on the thermal hydraulic performance of a 30 kW class OTEC system using an ammonia/water mixture. The performance of the embossed plate evaporator used in Case-I was also compared with that of the shell-and-plate evaporator equipped with herringbone plates used in Case-II. The principal findings are summarized as follows.

1. Under the tested conditions, Case-I maintained a higher evaporation pressure and produced a higher turbine power output than Case-II. The lower pressure drop on the cold water side in Case-I reduced the associated pumping power requirement. However, the two cases differed in heat transfer area, gas–liquid separator configuration, internal flow channel geometry, and plate characteristics. In addition, structural deformation of the Case-II plates was observed. Therefore, the measured performance differences should be interpreted as a system level comparison between the two experimental configurations and cannot be attributed solely to the embossing geometry of the plates.
2. Increasing the working fluid flow rate generally increased the overall heat transfer coefficients of the evaporator and condenser owing to the increased mass flux on the working fluid side. At the same time, it increased parasitic power consumption and decreased the calculated vapor separation ratio. Furthermore, the temperature variation in the ammonia/water mixture within the heat exchangers decreased as the working fluid flow rate increased, thereby reducing the thermodynamic benefit associated with the temperature glide of the non-azeotropic mixture. These competing effects resulted in a trade off between enhanced heat transfer and net power output.
3. Among the discrete working fluid flow rates tested (5, 6, 7, 8, 9, 10, and 12 t/h), the highest net power output was obtained at 6 t/h. At warm and cold water flow rates of 400 m^3/h and a working fluid flow rate of 6 t/h, the evaporator overall heat transfer coefficient, turbine power output, and net power output were 1.15 kW/(m^2·K), 32.2 kW, and 15.6 kW, respectively. The 16.6 kW difference between the turbine and net power outputs demonstrates the substantial effect of the pumping power requirements included within the defined system boundary. The working fluid flow rate of 6 t/h was the best performing value among the discrete flow rates tested; however, this result does not establish the precise continuous optimum.
4. Increasing either the warm or cold water flow rate from 400 to 500 m^3/h increased the turbine power output by approximately 10%, but the associated increase in pumping

power resulted in a decrease in net power output. Furthermore, the vapor flow rate at the turbine inlet approached a plateau above approximately 8 t/h because the vapor separation ratio decreased with increasing total working fluid flow rate. Therefore, maximizing the overall heat transfer coefficient alone does not maximize the net power output. Maximizing net power output requires the simultaneous consideration of heat transfer performance, pressure losses, vapor separation behavior, turbine inlet conditions, temperature glide, and auxiliary pumping power.

Several limitations should be considered when interpreting these results. The working fluid flow rate was examined only at discrete test points, and the Case-I and Case-II configurations differed in several design parameters. In addition, heated and cooled freshwater streams were used to simulate the warm and cold seawater heat sources, respectively, and the effects of long term operation with actual seawater, including biofouling and corrosion, were not evaluated. The uncertainty analysis was conducted primarily under the baseline operating condition, and the external piping losses and power consumption of some auxiliary components were excluded from the defined system boundary.

Future studies should conduct experiments using more closely spaced working fluid flow rates near 6 t/h to determine the optimum operating point more precisely. Additional studies should also isolate the effects of the plate surface geometry from those of the heat transfer area and separator configuration. Long term experiments using actual seawater are required to evaluate biofouling, corrosion, and performance degradation. Finally, dynamic flow control methods that respond to variations in seawater temperature and flow rate should be developed and validated under realistic operating conditions.

Author Contributions: Conceptualization, Y.I.; methodology, Y.I., J.I., H.G. and T.M.; software, J.I., H.G. and T.M.; validation, Y.I., J.I., H.G. and T.M.; investigation, J.I., H.G. and T.M.; data curation, J.I., H.G. and T.M.; writing—original draft preparation, Y.I. and T.M.; writing—review and editing, Y.I. and T.M.; visualization, T.M.; supervision, Y.I.; project administration, T.M. All authors have read and agreed to the published version of the manuscript.

Funding: This research received no external funding.

Data Availability Statement: The data presented in this study are available on request from the corresponding author.

Conflicts of Interest: The authors declare no conflicts of interest.

Nomenclature

A	heat transfer area, [m^2]
C	heat capacity flow rate [kW/K]
c_p	specific heat, [J/kg/K]
h	specific enthalpy, [J/kg]
m	mass flow rate, [kg/s or t/h]
P	pressure, [MPa]
Q	heat flow rate, [kW or MW]
s	specific entropy, [J/kg/K]
T	absolute temperature [K] in Equation (14); temperature [°C] elsewhere unless otherwise specified
ΔP	pressure drop, [kPa]
ΔT	temperature change, [K or °C]
ΔT_m	logarithmic mean temperature difference, [K or °C]
U	overall heat transfer coefficient, [kW/m^2/K]
$\dot{V}$	volumetric flow rate, [m^3/h]
W	power output, [kW]

Greek Symbols

η	efficiency, [%]
ρ	density, [kg/m^3]
ξ	vapor separation ratio [–]

Subscripts

B	boiling point
C	condenser
CS	cold source
E	evaporator
I	inlet
L	liquid
m	maximized
net	net
O	outlet
P	pump
sat	saturated
T	turbine
th	thermodynamic
V	vapor
WF	working fluid
WS	warm source
1–15	state point number in OTEC experimental plant

References

1. Ikegami, Y.; Uehara, H. Optimum design point for a closed-cycle OTEC system. In Proceedings of the 4th International Offshore and Polar Engineering Conference, Osaka, Japan, 10–15 April 1994; pp. 383–389.
2. Sun, F.; Ikegami, Y.; Jia, H.; Arima, H. Optimization design and exergy analysis of organic Rankine cycle in ocean thermal energy conversion. *Appl. Ocean Res.* **2011**, *33*, 290–298. [CrossRef]
3. William, H.A.; Chih, W. *Renewable Energy from the Ocean: A Guide to OTEC*; Oxford University Press: Oxford, UK, 1994.
4. Langer, J.; Quist, J.; Blok, K. Recent progress in the economics of ocean thermal energy conversion: Critical review and research agenda. *Renew. Sustain. Energy Rev.* **2020**, *130*, 109960. [CrossRef]
5. Melikoglu, M. Current status and future of ocean energy sources: A global review. *Ocean Eng.* **2018**, *148*, 563–573. [CrossRef]
6. Khan, N.; Kalair, A.; Abas, N.; Haider, A. Review of ocean tidal, wave and thermal energy technologies. *Renew. Sustain. Energy Rev.* **2017**, *72*, 590–604. [CrossRef]
7. Chen, H.; Goswami, D.Y.; Stefanakos, E.K. A review of thermodynamic cycles and working fluids for the conversion of low-grade heat. *Renew. Sustain. Energy Rev.* **2010**, *14*, 3059–3067. [CrossRef]
8. Panchal, C.B.; Rabas, T.J. *Thermal Performance of Advanced Heat Exchangers for Ammonia Vaporization and Condensation*; Technical Report ANL/ESD/TM-59; Argonne National Laboratory: Argonne, IL, USA, 1993.
9. Kalina, A.I. Combined cycle system with novel bottoming cycle. *J. Eng. Gas Turbines Power* **1984**, *106*, 737–742. [CrossRef]
10. Wall, G.; Chuang, C.C.; Ishida, M. Exergy study of the Kalina cycle. *ASME AES* **1989**, *10*, 73–77.
11. El-Sayed, Y.M.; Tribus, M.A. Theoretical comparison of the Rankine and Kalina cycles. *ASME Publ. AES* **1985**, *1*, 97–102.
12. Valdimarsson, P.; Eliasson, L. Factors influencing the economics of the Kalina power cycle. In Proceedings of the International Geothermal Conference, Reykjavik, Iceland, 14–17 September 2003; pp. 32–40.
13. Mirolli, M.D. Cementing Kalina cycle effectiveness. *IEEE Ind. Appl. Mag.* **2006**, *12*, 60–64. [CrossRef]
14. Nasruddin; Utama, R.U.; Rifaldi, M.; Noor, A. Energy and exergy analysis of kalina cycle system (KCS) 34 with mass fraction ammonia-water mixture variation. *J. Mech. Sci. Technol.* **2009**, *23*, 1871–1876. [CrossRef]
15. Guzović, Z.; Lončar, D.; Ferdelji, N. Possibilities of electricity generation in the Republic of Croatia by means of geothermal energy. *Energy* **2010**, *35*, 3429–3440. [CrossRef]
16. Mokarram, N.H.; Mosaffa, A.H. A comparative study and optimization of enhanced integrated geothermal flash and Kalina cycles: A thermoeconomic assessment. *Energy* **2018**, *162*, 111–125. [CrossRef]
17. Xu, F.; Goswami, D.Y. Thermodynamic properties of ammonia–water mixtures for power-cycle applications. *Energy* **1999**, *24*, 525–536. [CrossRef]
18. Uehara, H.; Ikegami, Y.; Fukukawa, H.; Uto, M. Performance Analysis of OTEC System Using Kalina Cycle: Thermodynamic Characteristics of Cycle. *Trans. JSME (Ser. B)* **1994**, *60*, 3519–3525. (In Japanese) [CrossRef]
19. Uehara, H.; Ikegami, Y.; Nishida, T. Performance Evaluation of Heat Exchangers in OTEC Using Ammonia/Water Mixture as Working Fluid. *Trans. JSME (Ser. B)* **1998**, *64*, 2750–2755. (In Japanese) [CrossRef]

20. Konagaya, M. Possibility of geothermal power generation using hot spring resources. *Policy Manag. Res.* **2007**, *4*, 1–10. (In Japanese)
21. DiPippo, R. Second Law assessment of binary plants generating power from low-temperature geothermal fluids. *Energy Build.* **2007**, *39*, 1080–1087. [CrossRef]
22. Braungart, S.; Fleuchaus, P. Review of geothermal and solar-boosted low-temperature power generation. *Geothermics* **2019**, *81*, 110–122. [CrossRef]
23. Matsuda, K. Power generation using heat of distillation column top gas. *Chem. Eng. Jpn.* **2009**, *73*, 423–425. (In Japanese)
24. Oehler, B.; Aumann, R. Operational experience of geothermal Kalina cycle power plants. *Geothermics* **2020**, *86*, 101800. [CrossRef]
25. Bombarda, P.; Invernizzi, C.M.; Pietra, C. Heat recovery from Diesel engines: Rankine vs Kalina cycles. *Energy* **2010**, *35*, 2700–2706. [CrossRef]
26. Ahamed, R.; Invernizzi, C.M. Heat transfer characteristic of non-azeotropic refrigerant mixtures in plate heat exchangers. *Int. J. Refrig.* **2016**, *69*, 112–123. [CrossRef]
27. Kim, J.S.; Kim, N.H. Pressure drop and flow boiling heat transfer of ammonia/water mixtures in chevron plate heat exchangers. *Int. J. Heat Mass Transf.* **2015**, *85*, 871–882. [CrossRef]
28. Zhang, X.R.; Yamaguchi, H. Performance analysis of a low-grade thermal energy conversion cycle using supercritical CO2. *Energy* **2007**, *32*, 573–579. [CrossRef]
29. Ayub, Z.H. Plate heat exchangers in ammonia systems: Design and field experience. *Heat Transf. Eng.* **2003**, *24*, 33–40. [CrossRef]
30. Li, L.; Guo, Y.; Zhang, B.; Guo, X. Experimental study on flow boiling in microchannel evaporators with top gap structures. *Int. J. Heat Mass Transf.* **2025**, *241*, 126710. [CrossRef]
31. Khan, M.S.; Lior, N. Thermodynamic and economic analysis of low-temperature energy recovery systems. *Energy* **2016**, *113*, 912–927. [CrossRef]
32. Valencia, G.; Núñez, J.; Duarte, J. Multiobjective optimization of a plate heat exchanger in a waste heat recovery organic Rankine cycle system for natural gas engines. *Entropy* **2019**, *21*, 655. [CrossRef] [PubMed]
33. Galezzo, D.C.; Silva, J.A. Hydraulic performance and parasitic losses in low-temperature heat recovery evaporators. *Appl. Therm. Eng.* **2020**, *178*, 115590. [CrossRef]
34. Yasunaga, T.; Ikegami, Y.; Monde, M. Performance evaluation of OTEC using shell and plate heat exchanger with ammonia/water mixture. *Trans. JSME (Ser. B)* **2008**, *74*, 445–451. (In Japanese) [CrossRef]
35. Bernardoni, C.; Binotti, M.; Giostri, A. Techno-economic optimization of OTEC power plants considering heat exchanger geometries. *Renew. Energy* **2019**, *132*, 1284–1296. [CrossRef]
36. Uehara, H. Ocean thermal energy conversion and piping technology. *Pip. Technol.* **1981**, *23*, 51–58. (In Japanese)
37. Yang, M.H.; Yeh, R.H. Optimization of heat exchanger area allocation for ocean thermal energy conversion systems. *Energy Convers. Manag.* **2022**, *251*, 114970. [CrossRef]
38. Ibrahim, O.M.; Klein, S.A.; Mitchell, J.W. Effects of irreversibility and economics on the performance of a heat engine. *J. Sol. Energy Eng.* **1992**, *114*, 267–271. [CrossRef]
39. Imran, M.; Park, B.S.; Kim, H.J. Multi-objective optimization of Organic Rankine Cycle systems for low-grade waste heat recovery. *Energy* **2018**, *157*, 468–481. [CrossRef]
40. Vera, D.; Jurado, F.; Panopoulos, K.D. Techno-economic assessment of biomass gasification combined with ORC and Kalina cycles. *Energy* **2020**, *202*, 117765. [CrossRef]
41. Zhang, L.; Xu, G.; Quan, Y. Dynamic modeling and control strategy for ocean thermal energy conversion systems under ocean thermal fluctuations. *Energy Convers. Manag.* **2023**, *285*, 117012. [CrossRef]
42. PROPATH Group. *PROPATH: A Program Package of Thermo-Physical Properties of Fluids, version 11.1*; PROPATH Group: Fukuoka, Japan, 2008.
43. Ikegami, Y.; Bejan, A. On the thermodynamic optimization of power plants with heat transfer and fluid flow irreversibilities. *J. Sol. Energy Eng.* **1998**, *120*, 134–144. [CrossRef]
44. Kline, S.J.; McClintock, F.A. Describing uncertainties in single-sample experiments. *Mech. Eng.* **1953**, *75*, 3–8.

Disclaimer/Publisher's Note: The statements, opinions and data contained in all publications are solely those of the individual author(s) and contributor(s) and not of MDPI and/or the editor(s). MDPI and/or the editor(s) disclaim responsibility for any injury to people or property resulting from any ideas, methods, instructions or products referred to in the content.